Optics Letters

Voltage-tunable Q factor in a photonic crystal microcavity

A. I. Krasnov,[1,2,†] P. S. Pankin,[1,2,†*] D. S. Buzin,[1,2,†] G. A. Romanenko,[1,3,4,†] V. S. Sutormin,[1,2] F. V. Zelenov,[4,5] A. N. Masyugin,[4,5] M. N. Volochaev,[1] S. Ya. Vetrov,[1,2] and I. V. Timofeev[1,2]

[1]Kirensky Institute of Physics, Krasnoyarsk Scientific Center, Siberian Branch, Russian Academy of Sciences, Krasnoyarsk 660036, Russia
[2]Siberian Federal University, Krasnoyarsk 660041, Russia
[3]Krasnoyarsk Scientific Center, Siberian Branch, Russian Academy of Sciences, Krasnoyarsk 660036, Russia
[4]Siberian State University of Science and Technology, Krasnoyarsk 660037, Russia
[5]AO NPP Radiosvyaz, Krasnoyarsk 660021, Russia
[†]These authors equally contributed to this work.
*Corresponding author: pavel-s-pankin@iph.krasn.ru

Received 27 October 2022; revised 20 February 2023; accepted 21 February 2023; posted 21 February 2023; published 22 March 2023

A photonic crystal microcavity with a tunable quality factor (Q factor) has been implemented on the basis of a bound state in the continuum using the advanced liquid crystal cell technology platform. It has been shown that the Q factor of the microcavity changes from 100 to 360 in the voltage range of 0.6 V.

https://doi.org/10.1364/OL.479431

Bound states in the continuum (BICs) are the nonradiative localized eigenmodes implemented in an open system. The BIC was first reported by von Neumann and Wigner in 1929 as a solution of the problem for a quantum particle in a finite oscillating potential [1]. The wave function of a particle is localized, while its energy is positive and lies within a continuum of propagating states. The BIC is a general wave phenomenon, which occurs not only in quantum mechanics, but also in radio physics, photonics, and acoustics [2–6]. Changing the parameters of a system near the BIC, one can control the coupling between a localized mode and the continuum of propagating waves and thereby tune the radiation component of the system quality factor (Q factor). In practice, due to the finite geometric length of structures, imperfection of fabrication techniques used, and absorption of materials, the amplitude of the Fano resonances with a finite Q factor [7–9] at the BIC points turns to zero. In this case, we can speak about the implementation of quasi-BICs. The BIC concept was used in various photonics applications, in particular, in lasers [10,11], sensors [12–15], waveguides [16,17], optical switches [18], nonlinear amplifiers [19], etc. According to the mechanism of implementation, the BICs are divided into several classes [2–6]. The symmetry-protected BICs (SP BICs) are based on opposite symmetries of localized modes and propagating waves, which yields the zero overlap integral [20,21]. The Friedrich–Wintgen (accidental) BICs (FW BICs) originate from the destructive interference of waves outgoing from a cavity [16,22]. According to Lee's theorem [23], in a one-dimensional (1D) multilayer model, the transmission zeros and, consequently, BICs, cannot be implemented. This theorem, however, is not generalized to the 1D multilayers of anisotropic materials, in which, as in the two-dimensional (2D) and three-dimensional (3D) models, the BICs were also implemented [24–26]. The authors of Refs. [27,28] demonstrated a trilayer waveguide consisting of birefringent materials, which supports the waveguide quasi-BICs. The rest of the 1D models that have been proposed to date are based on photonic crystals (PhCs) with an anisotropic defect layer [29–34]. In this study, an optical microcavity model [30] with a voltage-tunable Q factor is implemented on the basis of a BIC. Figure 1(a) shows a microcavity consisting of two identical mirrors formed from 1D PhCs separated by a liquid crystal (LC) resonator layer.

The PhCs were formed on glass substrates pre-coated with aluminum-doped zinc oxide (AZO) with a refractive index (RI) of $n_{AZO} = 1.8 + i0.062$ [35] (hereinafter, the RIs of all the materials are given for a wavelength of $\lambda = 570$ nm) and a thickness of $d_{AZO} = 100$ nm. The PhC includes $N = 8$ periods consisting of a silicon nitride (Si_3N_4) layer and a silicon dioxide (SiO_2) layer formed by plasma-enhanced chemical vapor deposition. The RIs and layer thicknesses are $n_{Si_3N_4} = 2.15$ [36], $d_{Si_3N_4} = 80$ nm and $n_{SiO_2} = 1.45$ [37], $d_{SiO_2} = 153$ nm. To achieve an agreement with the measured spectra, the RIs were fitted in the range less than 5%. To obtain the symmetry, the PhC was additionally coated with an unpaired Si_3N_4 layer. Polyvinyl alcohol (PVA) layers with an RI of $n_{PVA} = 1.48$ [38] and a thickness of $d_{PVA} = 100$ nm were formed on each PhC by the spin-coating method. The mechanical rubbing of the PVA layers ensured a homogeneous planar alignment of the LC. The PhC mirrors were placed into a metal holder with tuning screws to make a uniform gap, which was determined by teflon spacers with a thickness of approximately $d = 9.57$ μm. The gap between PhC mirrors was filled by 4-pentyl-4'-cyanobiphenyl (5CB) nematic LC with RIs of $n_\perp = \sqrt{\varepsilon_\perp} = 1.55$ and $n_\parallel = \sqrt{\varepsilon_\parallel} = 1.74$ [39–41] by a capillary method. The preferred alignment of the long axes of LC molecules is described by the unit vector $\boldsymbol{a} = [\cos(\phi)\cos(\theta), \sin(\phi)\cos(\theta), \sin(\theta)]$, which is called

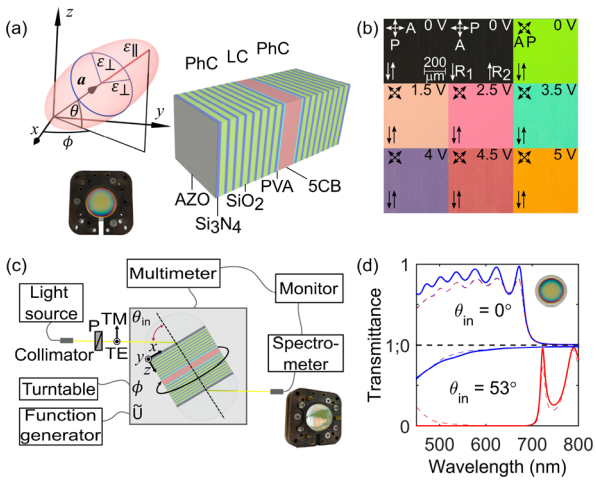

Fig. 1. (a) PhC microcavity model. The inset shows the orientation of an LC permittivity ellipsoid. The microcavity is presented in the photograph. (b) Polarizing optical microscope images of the LC layer texture taken in crossed polarizers at different applied voltages. Here R_1 and R_2 are the PVA rubbing directions. Crossed double arrows show the direction of the polarizer (P) and analyzer (A). (c) Scheme for measuring the microcavity transmittance spectra. The transverse electric (TE) and transverse magnetic (TM) vectors show the direction of the electric field at the corresponding polarizations. The photograph in the inset shows the microcavity with hemispherical lenses. (d) Measured (dashed line) and calculated (solid line) PhC transmittance spectra for the TE (red) and TM (blue) waves. The top and bottom plots correspond to the normal incidence of light and the incidence at the Brewster's angle, respectively. The photograph of the PhC is shown in the inset.

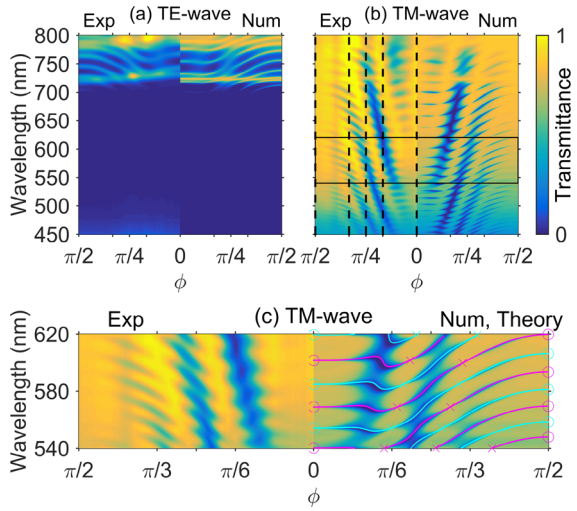

Fig. 2. Transmittance spectra of the optical microcavity at different azimuthal angles ϕ of the LC OA for (a) TE and (b),(c) TM waves. The left-hand subpanels show the measured spectra and the right-hand subpanels present the calculated ones. The black rectangle in (b) is shown in close-up in (c). The vertical dashed lines ($\phi = 0, \pi/6, \pi/4, \pi/3, \pi/2$) in (b) correspond to the spectra in Fig. 3 at applied voltage U = 0 V. Solid lines in (c) correspond to the solutions of the problem on the eigenvalues of an open cavity for the even (magenta lines) and odd (cyan lines) modes. The solutions are shown by circles for the SP BIC problem and by crosses for FW BIC problem.

the director [42]. In nematic LC the director coincides with the orientation of optical axis (OA) determined, according to Fig. 1(a), as a direction of the major semiaxis of the permittivity ellipsoid.

Figure 1(b) presents polarizing microscopy images of the optical texture of the LC layer. When the rubbing direction is parallel to the polarizer or analyzer, a uniform dark texture can be seen. The maximum intensity of the transmitted light is observed upon rotation of the crossed polarizers by 45° [the top row in Fig. 1(b)]. These optical textures confirm the planar LC alignment. The conducting transparent AZO layers make it possible to apply 1 kHz AC voltage to the LC layer to avoid blocking of the external field by ions in the LC. It can be seen in Fig. 1(b) (the middle and bottom rows) that the applied voltage changes the color of the optical texture of the LC layer, which is evidence of the change in the LC orientational structure. Figure 1(c) presents a scheme for measuring the microcavity transmittance spectra. The incoherent radiation of a halogen lamp from a Thorlabs OSL2 source propagates through an optical fiber and focuses with a collimator in a spot approximately 2 mm in diameter. After the transmittance through a polarizer, the TE-polarized (TE wave) or TM-polarized (TM wave) radiation passes into the microcavity through hemispherical glass lenses with an RI of $n_G = 1.5$. The lenses are glued to the glass substrates of the microcavity using immersion oil with an RI of $n_{Oil} = 1.5$ to eliminate an air gap. Introducing the radiation through the glass lenses at an angle of $\theta_{in} = \arcsin\left[(n_{Si_3N_4}/n_G)\sin\left(\arctan\left(n_{SiO_2}/n_{Si_3N_4}\right)\right)\right] \approx 53°$, one can implement the Brewster effect for the TM wave at the Si_3N_4/SiO_2 interfaces [43]. The outgoing radiation is collected in a fiber optic collimator connected to an OCEAN FX-UV-VIS spectrometer. The microcavity is mounted on an Thorlabs KPRM1E/M motorized precision rotation stage, which makes it possible to change the azimuthal angle ϕ of the LC OA orientation. The external voltage applied to the LC layer using an Aktakom AWG-4150 function generator can change the polar angle θ of the LC OA orientation. The value and frequency of the applied voltage are controlled with an Aktakom ABM-4552 multimeter. The operation of all the units and recording of the spectra are monitored using a personal computer (PC). Figure 1(d) presents the PhC transmittance spectra measured and calculated by the Berreman transfer matrix method [44]. It can be seen that, under normal incidence of light, there is a photonic bandgap (PBG) with the center at $\lambda_{PBG} = 800$ nm for both the TE and TM waves. When the light falls at the Brewster's angle, the PBG shifts to the visible range and $\lambda_{PBG} = 570$ nm for the TE wave. The PBG for the TM wave vanishes due to the Brewster effect. Thus, in a certain wavelength range, the PhC is nontransparent for the TE waves and transparent for the TM ones.

Figure 2 illustrates the transformation of the transmittance spectra of the microcavity filled with the LC upon variation in the azimuthal angle ϕ of the LC OA orientation. Figure 2(a) shows that the spectrum does not change in the PBG region for the TE waves, which demonstrates the absence of evident resonances due to the absorption in LC. On the other hand, the spectrum for the TM waves contains numerous resonant lines in the same spectral range [see Fig. 2(b)]. The rotation of the LC OA causes the change in the position and width of the resonant lines. It is the consequence of the changes both in the optical width of the LC layer and in the coupling between the localized modes and the waves propagating in the

PhC waveguides. The behavior of the spectra can be qualitatively explained by dividing the total electric field strength $\boldsymbol{E}$ of light in the LC into contributions of the ordinary wave (o wave) $\boldsymbol{E}_o$ and extraordinary wave (e wave) $\boldsymbol{E}_e$: $\boldsymbol{E} = \boldsymbol{E}_e + \boldsymbol{E}_o$. The polarization directions of the o and e waves are given by the vectors $\boldsymbol{E}_o = E_o[\boldsymbol{a} \times \boldsymbol{\kappa}_o]$ and $\boldsymbol{E}_e = E_e\left[\boldsymbol{a} - \frac{\varepsilon_e(\alpha)}{\varepsilon_o}\boldsymbol{\kappa}_e(\boldsymbol{\kappa}_e\boldsymbol{a})\right]$ [45], respectively. Here, $\boldsymbol{\kappa}_{o,e} = [\kappa_{o,ex}; 0; \kappa_{o,ez}]$ is the unit vector along the direction of propagation of the o, e wave; $\varepsilon_o = \varepsilon_\perp$ is the permittivity for the o wave, and $\varepsilon_e(\alpha)$ is the permittivity for the e wave, which has the values $\varepsilon_\perp \le \varepsilon_e(\alpha) \le \varepsilon_\parallel$ and is determined by the angle α between the vectors $\boldsymbol{a}$ and $\boldsymbol{\kappa}_e$. Since the o and e waves have different permittivities, they have different phase incursions during propagation through the LC layer. In the general case, for the angles $\phi \neq 0$ and $\theta \neq 0$, all the components of the o and e waves are nonzero: $\boldsymbol{E}_{o,e} = [E_{o,ex}, E_{o,ey}, E_{o,ez}]$; i.e., the TE and TM waves are mixed in the LC layer. The measured and calculated spectra in Fig. 2(b) show that the resonant lines collapse at $\phi = 0$ and $\phi = \pi/2$. The positions of the collapses coincide with the solutions of the problem on the SP BICs [30], which are shown by circles in Fig. 2(c). At $\theta = 0$ and $\phi = 0$, the o wave has a projection only on the TE wave: $\boldsymbol{E}_o = [0, E_{oy}, 0]$ and the e wave has a projection only on the TM wave: $\boldsymbol{E}_e = [E_{ex}, 0, E_{ez}]$ [see Figs. 1(a) and 1(b)]. At $\theta = 0$ and $\phi = \pi/2$, the situation is opposite: $\boldsymbol{E}_o = [E_{ox}, 0, E_{oz}]$, $\boldsymbol{E}_e = [0, E_{ey}, 0]$. This means that, in these cases, the propagating TM wave is not converted into the TE wave, which can be localized due to the PBG. This explains qualitatively also the redshift of the resonant lines in Fig. 2(b) with increasing angle ϕ. For the localized TE waves with only a y component, the RI changes from the minimum value $n|_{\phi=0}^{\theta=0} = n_\perp$ to the maximum one $n|_{\phi=\pi/2}^{\theta=0} = n_\parallel$. The behavior of the resonant lines is confirmed also by the numerical calculation and solution of the problem on the eigenvalues of an open system [30]. Figure 2(c) shows the spectral position of the resonances $\lambda_0 = 2\pi/\omega_0$ obtained from the eigenvalue $\omega_r = \omega_0 - i\gamma$.

The collapse of the resonant lines can be observed also at the intermediate angles $\phi \neq 0, \pi/2$. The positions of the collapses coincide with the solutions of the problem on the FW BICs [30] shown by crosses in Fig. 2(c). When the total projection of the contributions of the o and e waves on the TM wave at the output of LC layer is zero $E_x = E_{ex} + E_{ox} = 0$, the energy cannot be brought out of the cavity by the propagating TM waves. This differentiates the SP BICs from the FW BICs, in which not only the TE component of the total field is localized in the LC layer due to the PBG, but also the TM component, due to the destructive interference of the waves at the output of the LC layer [30]. As it was shown in Refs. [30,34], the LC layer in this case plays the role of a full-wave phase plate, which recovers the state of polarization at the output identical to that at the input [46]. In both cases, when the SP BICs or FW BICs are implemented, there is no coupling between the localized and propagating waves, which makes the radiation component of the imaginary part of the eigenvalue zero, $\gamma_{rad} = 0$; $\gamma = \gamma_{rad} + \gamma_{ext}$. In the spectrum it appears as a vanishing amplitude of the resonant line, the width of which at the quasi-BIC point is only determined by the nonradiative extinction loss, including the absorption and scattering $\Delta\omega = 2\gamma_{ext}$. Between the two angles ϕ corresponding to the BIC implementation, the radiation component of the resonant linewidth γ_{rad} changes from zero to the finite value and *vice versa*. It allows us to consider this situation as the implementation of the resonances with the tunable quality factor $Q = \omega_0/2\gamma$.

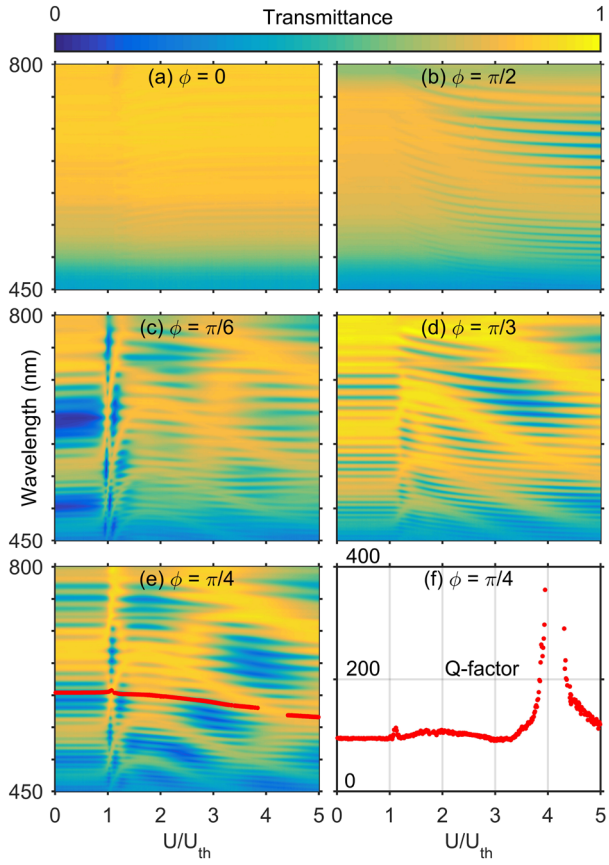

Fig. 3. (a)–(e) Measured transmittance spectra of the optical microcavity at different values of applied voltages U; $U_{th} \approx 1.2$ V is the threshold voltage for LC reorientation. (f) Q factor of the resonant line [red dots in (e)] calculated from the full width at half maximum (FWHM).

Figure 3 illustrates the transformation of the transmittance spectra of the microcavity upon variation in the voltage applied to the LC layer at constant azimuthal angles ϕ of the LC OA orientation. It can be seen from the spectra that, at the voltages below the threshold value of the Fredericks effect [42] U<U_{th}, the positions and widths of the resonant lines do not change. The voltage $U = U_{th}$ corresponds to the beginning of the LC reorientation. With a further increase in the voltage $U \ge U_{th}$, the director rotates toward the external electric field direction (along the z axis); i.e., the polar angle θ increases [see Fig. 1(a)]. At $\phi = 0$, for any polar angle θ, the o wave has a projection only on the TE wave, while the e wave has a projection only on the TM wave. The propagating TM wave is not converted to the TE wave at any applied voltage U. Therefore, the weak resonances in Fig. 3(a), which have fixed widths, correspond to the localized TM waves. They arise due to the low reflectance at the interface between the PVA layer and the first Si_3N_4 layer. These resonances, as a background of the resonances with the tunable Q factor, can also be seen in Fig. 3(b) up to the threshold voltage, as well as in Figs. 2(b) and 2(c) at $\phi = 0, \pi/2$. Intermixing of the TE and TM waves in the LC layer in the general case of $\phi \neq 0$ and $\theta \neq 0$ leads to the occurrence of the resonances with the tunable Q factor, as can be seen in Figs. 3(b)–3(e). At certain voltages U, one can see the collapse of the resonant lines corresponding to the FW BICs (the mechanism of their implementation was

explained above). At an external voltage of $U>5U_{th}$, the resonant lines in the spectrum remain almost invariable. This is due to the fact that, at high voltages, the LC director, except for the thin surface layer, aligns along the applied field direction [42]. This explains also the blueshift of the resonant lines, since, in the limit case of high voltages, the angle is $\theta = \pi/2$ and for the localized TE wave, which has only the y component, the LC RI is equal to the minimum value $n|_{\phi}^{\theta=\pi/2} = n_{\perp}$ [Fig. 1(a)]. In Fig. 3(f), the Q factor is presented for one of the resonant lines from Fig. 3(e). It can be seen that the Q factor sharply increases upon approaching the FW BIC in the vicinity of $U \approx 4.1U_{th}$. The measured Q factor changes from 100 to 360 in the voltage range from $3.4U_{th}$ to $3.9U_{th}$, i.e., by $0.5U_{th} = 0.6$ V. The sensitivity of the Q factor to the change in the applied voltage is $\Delta Q/\Delta U = 433$ V^{-1}. Thus, a photonic crystal microcavity with a liquid crystal defect layer was created, where on the basis of the concept of the bound state in the continuum, we first demonstrated the efficient voltage control by both the position [47–51] and width of the resonant lines. The proposed model with the voltage-tunable Q factor can be used for energy-efficient design of low-threshold dye microlasers [49], perfect light absorbers [33], biophotonic sensors [52].

Funding. Russian Science Foundation (22-22-00687).

Acknowledgments. The authors are grateful to Dmitrii N. Maksimov and Sergey A. Myslivets for fruitful discussions. The authors thank the Krasnoyarsk Regional Center of Research Equipment of FRC KSC SB RAS for providing the equipment. This study was supported by the Russian Science Foundation, project no. 22-22-00687.

Disclosures. The authors declare no conflicts of interest.

Data availability. The data that support the findings of this study are available from the corresponding author, P.S.P., upon reasonable request.

REFERENCES

1. J. von Neumann and E. P. Wigner, Phys. Zeitschrift **30**, 467 (1929).
2. C. W. Hsu, B. Zhen, A. D. Stone, J. D. Joannopoulos, and M. Soljačić, Nat. Rev. Mater. **1**, 16048 (2016).
3. A. F. Sadreev, Reports on Progress in Physics **84**, 055901 (2021).
4. K. L. Koshelev, Z. F. Sadrieva, A. A. Shcherbakov, Y. Kivshar, and A. A. Bogdanov, Phys.-Usp. **1**, 1 (2021).
5. S. I. Azzam and A. V. Kildishev, Adv. Opt. Mater. **9**, 2001469 (2021).
6. S. Joseph, S. Pandey, S. Sarkar, and J. Joseph, Nanophotonics **10**, 4175 (2021).
7. M. F. Limonov, M. V. Rybin, A. N. Poddubny, and Y. S. Kivshar, Nat. Photonics **11**, 543 (2017).
8. M. V. Rybin, K. L. Koshelev, Z. F. Sadrieva, K. B. Samusev, A. A. Bogdanov, M. F. Limonov, and Y. S. Kivshar, Phys. Rev. Lett. **119**, 243901 (2017).
9. Z. Zhao, C. Guo, and S. Fan, Phys. Rev. A **99**, 033839 (2019).
10. A. Kodigala, T. Lepetit, Q. Gu, B. Bahari, Y. Fainman, and B. Kanté, Nature **541**, 196 (2017).
11. C. Huang, C. Zhang, S. Xiao, Y. Wang, Y. Fan, Y. Liu, N. Zhang, G. Qu, H. Ji, J. Han, L. Ge, Y. Kivshar, and Q. Song, Science **367**, 1018 (2020).
12. A. M. Chernyak, M. G. Barsukova, A. S. Shorokhov, A. I. Musorin, and A. A. Fedyanin, JETP Lett. **111**, 46 (2020).
13. I. Yusupov, D. Filonov, A. Bogdanov, P. Ginzburg, M. V. Rybin, and A. Slobozhanyuk, Appl. Phys. Lett. **119**, 193504 (2021).
14. C. Schiattarella, G. Sanità, B. G. Alulema, V. Lanzio, S. Cabrini, A. Lamberti, I. Rendina, V. Mocella, G. Zito, and S. Romano, Biosens. Bioelectron.: X **12**, 100262 (2022).
15. A. Sadreev, E. Bulgakov, A. Pilipchuk, A. Miroshnichenko, and L. Huang, Phys. Rev. B **106**, 085404 (2022).
16. C. W. Hsu, B. Zhen, J. Lee, S. L. Chua, S. G. Johnson, J. D. Joannopoulos, and M. Soljačić, Nature **499**, 188 (2013).
17. E. A. Bezus, D. A. Bykov, and L. L. Doskolovich, Photonics Res. **6**, 1084 (2018).
18. D. N. Maksimov, A. S. Kostyukov, A. E. Ershov, M. S. Molokeev, E. N. Bulgakov, and V. S. Gerasimov, "Thermo-optic hysteresis with bound states in the continuum," arXiv, arXiv:2210.02364v1 (2022).
19. K. Koshelev, S. Kruk, E. Melik-Gaykazyan, J.-H. Choi, A. Bogdanov, H.-G. Park, and Y. Kivshar, Science **367**, 288 (2020).
20. E. N. Bulgakov and A. F. Sadreev, Phys. Rev. B **78**, 075105 (2008).
21. D. C. Marinica, A. G. Borisov, and S. V. Shabanov, Phys. Rev. Lett. **100**, 183902 (2008).
22. H. Friedrich and D. Wintgen, Phys. Rev. A **32**, 3231 (1985).
23. H. W. Lee, Phys. Rev. Lett. **82**, 2358 (1999).
24. F. Razzaz and M. A. S. Alkanhal, IEEE Photonics J. **10**, 6100112 (2018).
25. I. Quotane, E. H. El Boudouti, and B. Djafari-Rouhani, Phys. Rev. B **97**, 024304 (2018).
26. S. Mizuno, Appl. Phys. Express **12**, 035504 (2019).
27. J. Gomis-Bresco, D. Artigas, and L. Torner, Nat. Photonics **11**, 232 (2017).
28. S. Mukherjee, J. Gomis-Bresco, D. Artigas, and L. Torner, Opt. Lett. **46**, 2545 (2021).
29. I. V. Timofeev, D. N. Maksimov, and A. F. Sadreev, Phys. Rev. B **97**, 024306 (2018).
30. P. S. Pankin, B.-R. Wu, J.-H. Yang, K.-P. Chen, I. V. Timofeev, and A. F. Sadreev, Commun. Phys. **3**, 91 (2020).
31. P. S. Pankin, D. N. Maksimov, K. P. Chen, and I. V. Timofeev, Sci. Rep. **10**, 13691 (2020).
32. D. O. Ignatyeva and V. I. Belotelov, Opt. Lett. **45**, 6422 (2020).
33. B. Wu, J. Yang, P. S. Pankin, C. Huang, W. Lee, D. N. Maksimov, I. V. Timofeev, and K. Chen, Laser Photonics Rev. **15**, 2000290 (2021).
34. P. S. Pankin, D. N. Maksimov, and I. V. Timofeev, J. Opt. Soc. Am. B **39**, 968 (2022).
35. I. A. Tambasov, M. N. Volochaev, A. S. Voronin, N. P. Evsevskaya, A. N. Masyugin, A. S. Aleksandrovskii, T. E. Smolyarova, I. V. Nemtsev, S. A. Lyashchenko, G. N. Bondarenko, and E. V. Tambasova, Phys. Solid State **61**, 1904 (2019).
36. K. Luke, Y. Okawachi, M. R. E. Lamont, A. L. Gaeta, and M. Lipson, Opt. Lett. **40**, 4823 (2015).
37. L. Gao, F. Lemarchand, and M. Lequime, J. Eur. Opt. Soc., Rapid publ. **8**, 13010 (2013).
38. M. J. Schnepf, M. Mayer, C. Kuttner, M. Tebbe, D. Wolf, M. Dulle, T. Altantzis, P. Formanek, S. Förster, S. Bals, T. A. F. König, and A. Fery, Nanoscale **9**, 9376 (2017).
39. J. Li, C. H. Wen, S. Gauza, R. Lu, and S. T. Wu, J. Disp. Technol. **1**, 51 (2005).
40. V. Tkachenko, G. Abbate, A. Marino, F. Vita, M. Giocondo, A. Mazzulla, F. Ciuchi, and L. D. Stefano, Mol. Cryst. Liq. Cryst. **454**, 263 (2006).
41. M. S. Sefton, A. R. Bowdler, and H. J. Coles, Mol. Cryst. Liq. Cryst. **129**, 1 (1985).
42. L. M. Blinov, *Structure and Properties of Liquid Crystals, Topics in applied physics* (Springer, 2010).
43. S. A. Akhmanov and S. Y. Nikitin, *Physical Optics* (Clarendon Press, 1997).
44. D. W. Berreman, J. Opt. Soc. Am. **62**, 502 (1972).
45. F. V. Ignatovich and V. K. Ignatovich, Usp. Fiz. Nauk **182**, 759 (2012).
46. B. E. A. Saleh and M. C. Teich, *Fundamentals of Photonics, Wiley Series in Pure and Applied Optics* (Wiley, 2007).
47. S. Y. Vetrov and A. V. Shabanov, J. Exp. Theor. Phys. **93**, 977 (2001).
48. R. Ozaki, T. Matsui, M. Ozaki, and K. Yoshino, Jpn. J. Appl. Phys. **41**, L1482 (2002).
49. R. Ozaki, T. Matsui, M. Ozaki, and K. Yoshino, Appl. Phys. Lett. **82**, 3593 (2003).
50. V. G. Arkhipkin, V. A. Gunyakov, S. A. Myslivets, V. Y. Zyryanov, V. F. Shabanov, and W. Lee, J. Exp. Theor. Phys. **112**, 577 (2011).
51. P. S. Pankin, V. S. Sutormin, V. A. Gunyakov, F. V. Zelenov, I. A. Tambasov, A. N. Masyugin, M. N. Volochaev, F. A. Baron, K. P. Chen, V. Y. Zyryanov, S. Y. Vetrov, and I. V. Timofeev, Appl. Phys. Lett. **119**, 161107 (2021).
52. A. H. Aly, D. Mohamed, M. A. Mohaseb, N. S. A. El-Gawaad, and Y. Trabelsi, RSC Adv. **10**, 31765 (2020).